

DIII-D research to provide solutions for ITER and fusion energy

C.T. Holcomb^{1,*}, for the DIII-D Team: J. Abbate², A. Abe², A. Abrams³, P. Adebayo-Ige⁴, S. Agabian⁵, S. Ahmed⁶, N. Aiba⁷, N. Akcay³, T. Akiyama³, R. Albosta⁸, P. Aleynikov⁹, S. Allen¹⁰, H. Anand³, J. Anderson³, Y. Andrew¹¹, M. Ashburn⁴, A. Ashourvan³, M. Austin¹², G. Avdeeva³, D. Ayala³, M. Ayub³, E. Bagdy³, S. Banerjee², K. Barada¹³, L. Bardoczi³, O. Bardsley¹⁴, J. Barr³, E. Bass¹⁵, A. Battey¹⁶, Z. Bayler¹⁷, L. Baylor¹⁸, T. Bechtel¹⁹, M. Beidler¹⁸, E. Belli³, T. Benedett¹³, Z. Bergstrom³, M. Berkel²⁰, T. Bernard³, N. Bertelli², R. Bielajew⁵, G. Bodner³, J. Boedo¹⁵, R. Boivin³, T. Bolzonella²¹, P. Bonoli⁵, A. Bortolon², S. Bose², M. Boyer², W. Boyes¹⁶, L. Bradley¹³, R. Brambila³, A. Braun¹⁶, D. Brennan²², S. Bringuier³, L. Brodsky³, M. Brookman², J. Brooks²³, D. Brower¹³, W. Brown², J. Buck²⁴, S. Buczek³, D. Burgess¹⁶, M. Burke¹⁰, K. Burrell³, J. Butt¹⁶, R. Buttery³, I. Bykov³, P. Byrne³, A. Cacheris⁴, K. Callahan¹³, J. Callen⁸, D. Campbell²⁵, J. Candy³, J. Canik¹⁸, L. Cappelli²⁶, T. Carlstrom³, R. Carr³, W. Carrig³, B. Carter²⁷, T. Carter¹³, I. Carvalho³, W. Cary³, L. Casali⁴, L. Ceelen²⁰, M. Cengher³, M. Cha³, R. Chaban²⁸, V. Chan²⁹, B. Chapman⁸, I. Char³⁰, J. Chen³¹, R. Chen³¹, J. Chen¹³, X. Chen³, Y. Chen¹⁵, J. Chiriboga²⁸, E. Cho³, G. Choi³⁸, W. Choi³, H. Choudhury¹⁶, S. Chowdhury¹³, C. Chrystal³, Y. Chung³⁰, R. Churchill², R. Clark³, M. Clement², J. Coburn³⁶, S. Coda³⁹, R. Coffee⁴⁰, C. Collins¹⁸, J. Colmenares-Fernandez³, W. Conlin²², R. Coon³, T. Cote¹⁹, A. Creely⁴¹, N. Crocker¹³, C. Crowe³, B. Crowley³, T. Crowley⁴², M. Curie¹², D. Curreli⁴³, A. Dal Molin⁴⁴, J. Damba¹³, E. Dart⁴⁵, A. Dautt-Silva³, K. Davda⁴, A. De¹⁹, N. de Boucaud³, Y. de Jong²⁰, P. DE VRIES⁴⁶, A. de-Villeroche⁴⁷, G. DeGrandchamp⁴⁸, J. deGrassie³, D. Demers⁴², S. Denk⁵, E. DeShazer³, S. Di Genova²⁶, A. Diallo², A. Dimits¹⁰, R. Ding³¹, S. Ding¹⁹, D. Donovan⁴, X. Du³, J. Dunsmore¹¹, A. Dupuy³, J. Duran⁴, A. Dvorak¹⁸, F. Effenberg², N. Eidietis³, D. Elder⁴⁹, D. Eldon³, Y. Elsey³, D. Ennis³⁷, K. Erickson², D. Ernst⁵, M. Fajardo⁵⁰, H. Farre-Kaga¹¹, M. Fenstermacher¹⁰, N. Ferraro², J. Ferron³, A. Feyrer⁵¹, P. Fimognari⁴², R. Finden³, D. Finkenthal⁵², R. Fitzpatrick¹², S. Flanagan³, B. Ford⁸, W. Fox², S. Freiburger¹⁶, L. Fu², K. Gage⁴⁸, V. Gajaraj², I. Garcia⁵, F. Garcia³, A. Garcia⁴⁸, M. Garcia Munoz⁵³, D. Garnier⁵, A. Garofalo³, A. Gattuso³, B. Geiger⁸, K. Gentle¹², Y. Ghai¹⁸, K. Gill⁸, F. Glass³, P. Gohil³, X. Gong³¹, J. Gonzalez-Martin⁴⁸, Y. Gorelov³, V. Graber⁵⁴, R. Granetz⁵, C. Gray³, C. Greenfield³, B. Grierson³, R. Groebner³, W. Grosnickle³, M. Groth⁵⁵, S. Gu¹⁹, H. Guo³, J. Guterl³, W. Guttenfelder², R. Hager², S. Hahn²⁸, M. Halfmoon¹², J. Hall⁵⁶, V. Hall-Chen⁵⁷, F. Halpern³, G. Hammett², X. Han⁸, C. Hansen⁵⁸, E. Hansen⁴⁸, J. Hanson¹⁶, M. Hanson¹⁵, A. Harris³, R. Harvey³³, S. Haskey², D. Hatch⁵⁹, W. Hayashi⁴⁸, A. Hayes⁴, W. Heidbrink⁴⁸, J. Herfindal¹⁸, J. Hicok³, E. Hinson⁸, T. Hisakado³, C. Holcomb¹⁰, C. Holland¹⁵, L. Holland³, E. Hollmann¹⁵, A. Holm⁵⁵, I. Holmes³, K. Holtrop³, R. Hong¹³, R. Hood³⁶, L. Horvath¹⁴, S. Houshmandyar³, N. Howard⁵, E. Howell³², W. Hu³¹, Y. Hu³¹, Q. Hu², Y. Huang⁶⁰, J. Huang³¹, A. Huang⁶¹, A. Hubbard⁵, J. Hughes⁵, D. Humphreys³, J. Hurtado⁶², A. Hyatt³, K. Imada⁶³, V. Izzo⁶⁴, A. Jalalvand⁶⁵, S. Jardin², A. Jarvinen⁶⁶, Y. Jeon²⁸, H. Ji²², X. Jian¹⁵, L. Jian¹⁵, Y. Jiang²,

* Author to whom any correspondence should be addressed.



Original content from this work may be used under the terms of the [Creative Commons Attribution 4.0 licence](https://creativecommons.org/licenses/by/4.0/). Any further distribution of this work must maintain attribution to the author(s) and the title of the work, journal citation and DOI.

C. Johnson¹⁸, J. Johnson⁵, M. Jones²⁴, S. Joung⁸, P. Jouzdani², E. Jung²², E. Kallenberg³, R. Kalling²⁵, D. Kaplan³, A. Kaptanoglu²⁶, D. Kellman³, J. Kennedy²⁷, F. Khabanov⁸, J. Kim²⁸, H. Kim²⁸, E. Kim²⁹, S. Kim²², K. Kim¹⁸, C. Kim³⁰, T. Kim³¹, J. King³², A. Kinsey³³, D. Kirk³⁴, D. Klasing⁴, A. Kleiner², M. Knolker³, M. Kochan³⁴, B. Koel²², J. Koenders²⁰, M. Koepke³⁵, R. Kolasinski³⁶, E. Kolemen², E. Kostadinova³⁷, M. Kostuk³, G. Kramer², R. Kube², N. Kumar⁶⁷, R. La Haye⁸³, F. Laggner², C. Lahban², H. Lan³¹, R. Landry⁵, R. Lantsov¹³, L. Lao³, C. Lasnier¹⁰, C. Lau¹⁸, R. Leccacorvi⁵, J. Leddy³², M. Lee⁸², S. Lee⁴, K. Lee⁴, R. Lee³, M. Lehnen⁴⁶, A. Leonard³, E. Leppink⁵, M. LeSher³, J. Lestz⁴⁸, J. Leuer³, N. Leuthold¹⁹, G. Li³¹, X. Li³¹, Y. Li³¹, L. Li⁸³, N. Li¹⁰, Z. Li¹⁹, D. Lin³, Z. Lin²², Z. Lin⁴⁸, Y. Lin⁵, E. Linsenmayer³, J. Liu³¹, D. Liu³, D. Liu²², C. Liu², Z. Liu⁷¹, Y. Liu³, C. Liu³, A. Loarte-Prieto⁴⁶, S. Loch³⁷, L. LoDestro¹⁰, N. Logan¹⁰, J. Lohr³, J. Lore¹⁸, U. Losada Rodriguez³⁷, J. Loughran²⁸, M. Lowell¹³, T. Luce⁴⁶, N. Luhmann, P. Lunia¹⁶, R. Lunsford², L. Lupin-Jimenez², A. Lvovskiy³, B. Lyons³, X. Ma³, J. MacDonald³, T. Macwan¹³, R. Maingi², M. Major⁸, L. Malhotra⁸, M. Margo³, C. Marini¹⁵, A. Marinoni⁵, A. Maris⁵, E. Martin¹⁸, J. Mateja⁴, R. Mattes⁴, R. Maurizio¹⁹, D. Mauzey², L. McAllister³, G. McArdle³⁴, J. McClenaghan³, K. McCollam⁸, G. McKee⁸, K. McLaughlin³, A. McLean¹⁰, V. Mehta³⁰, E. Meier⁸¹, S. Meitner¹⁸, J. Menard², O. Meneghini³, G. Merlo¹², S. Messer⁴, W. Meyer¹⁰, C. Michael¹³, D. Miller³, M. Miller⁵, J. Mitchell¹⁴, E. Mitra²², C. Moeller³, M. Mohamed⁵, S. Molesworth¹⁵, K. Montes⁵, S. Mordijk²⁸, S. Morosohk⁵⁴, A. Moser³, D. Mueller², S. Munaretto², C. Murphy³, C. Muscatello³, R. Myers⁸, A. Nagy², D. Nath, M. Navarro⁸, R. Nazikian³, T. Neiser³, A. Nelson¹⁶, P. Nesbet³, F. Nespola², P. Nguyen³, D. Nguyen³, R. Nguyen³, J. Nichols¹⁸, M. Nocente, L. Nuckols¹⁸, R. Nygren³⁶, T. Odstrcil³, M. Okabayashi², E. Olofsson³, D. Orlov¹⁵, D. Orozco³, N. Osborne, T. Osborne³, F. OShea⁴⁰, D. Pace³, D. Packard³, A. Pajares Martinez³, C. Pakosta³, C. Pan³¹, M. Pandya⁸, D. Panici²², A. Pankin², Y. Park¹⁶, J. Park¹⁸, J. Park², C. Parker³, S. Parker⁶⁷, P. Parks³, M. Parsons⁶⁸, S. Paruchuri⁵⁴, C. Paz-Soldan¹⁶, T. Pederson³, W. Peebles¹³, B. Penafior³, E. Perez⁸, L. Periasamy³, R. Perillo¹⁵, C. Petty³, M. Pharr¹⁶, D. Pierce³, C. Pierren⁸, S. Pierson⁵, A. Pigarov³³, L. Pigatto²¹, D. Piglowski³, S. Pinches⁴⁶, R. Pinsky³, R. Pitts⁴⁶, J. Pizzo⁸, M. Podesta², Z. Popovic¹⁹, M. Porkolab⁵, Q. Pratt¹³, G. Prechel⁴⁸, I. Pusztai⁶⁹, P. Puthan-Naduvakkate¹⁹, J. Qian³¹, X. Qin⁸, O. Ra⁷⁰, T. Raines², K. Rakers⁸, K. Rath⁹, J. Rauch³, C. Rea⁵, R. Reed², A. Reiman², M. Reinke⁴¹, R. Reksoatmodjo²⁸, Q. Ren³¹, J. Ren⁴, Y. Ren², M. Rensink¹⁰, T. Rhodes¹³, N. Richner¹⁹, J. Ridzon⁵, G. Riggs³⁵, J. Riquezes¹⁶, P. Rodriguez Fernandez⁵, T. Rognlien¹⁰, G. Ronchi¹⁸, L. Rondini¹⁶, R. Rosati⁵, A. Rosenthal⁵, M. Ross³, J. Rost⁵, A. Rothstein²², J. Roveto⁷¹, J. Ruane³, D. Rudakov¹⁵, R. Rupani³, G. Rutherford⁵, S. Sabbagh¹⁶, J. Sachdev², N. Sadeghi¹³, A. Salmi⁶⁶, F. Salvador⁷², B. Sammulu³, C. Samuel¹⁰, A. Sandorfi⁷³, C. Sang⁷⁴, D. Santa⁷⁵, J. Sarff⁸, O. Sauter³⁹, H. Savelli⁵, C. Schaefer⁸, H. Schamis⁶⁸, J. Schellpfeffer⁸, D. Schissel³, L. Schmitz¹³, O. Schmitz⁸, P. Schroeder³, K. Schultz³, E. Schuster⁵⁴, F. Sciortino⁹, F. Scotti¹⁰, J. Scoville³, A. Seltzman⁵, J. Seo²², J. Serrano¹³, I. Sfiligoi¹⁵, M. Shafer¹⁸, R. Shapov³, H. Shen³, N. Shi³, D. Shiraki¹⁸, B. Short³, R. Shousha²², H. Si³¹, C. Sierra²⁷, G. Sinclair³, P. Sinha², G. Sips³, C. Skinner², T. Slendebroek¹⁹, J. Slief²⁰, R. Smirnov¹⁵, S. Smith³, D. Smith⁸, G. Snoep²⁰, P. Snyder¹⁸, W. Solomon³, X. Song⁵⁴, A. Sontag⁸, V. Soukhanovskii¹⁰, D. Spong¹⁸, J. Squire³, G. Staebler³, L. Stagner³, T. Stange⁹, P. Stangeby⁴⁹, E. Starling¹⁹, S. Stewart⁸, T. Stoltzfus-Dueck², S. Storment¹³, E. Strait³, D. Su³, L. Sugiyama⁵, P. Sun³¹, Y. Sun³¹, Y. Sun³¹, X. Sun¹⁹, C. Sung⁷⁶, W. Suttrop⁹, Y. Suzuki⁷⁷, R. Sweeney⁵, B. Taczak⁷⁸, Y. Takemura⁷⁹, S. Tang¹⁵, S. Tang¹⁹, W. Tang²², G. Tardini⁹, D. Taussig³, K. Teixeira³, K. Thackston³, D. Thomas³, K. Thome³, Y. Tinguely⁵, M. Tobin¹⁶, J. Tooker³, A. Torrezan de Sousa³, P. Traverso³⁷, G. Trevisan²⁹, E. Trier¹⁴, D. Truong³⁶, C. Tsui¹⁵, F. Turco¹⁶, A. Turnbull³, L. Turner⁴, E. Unterberg¹⁸, B. Van Compernelle³, R. van Kampen²⁰, M. Van Zeeland³, B. Victor¹⁰, R. Vieira⁵, E. Viezzer⁵³, S. Vincena¹³, D. Vollmer³, J. Wai²², M. Walker³, R. Waltz³, W. Wampler³⁶, L. Wang³¹, Y. Wang³¹, H. Wang³, Z. Wang⁵⁴, G. Wang¹³, A. Wang⁵, J. Watkins³⁶, M. Watkins³,

T. Watts¹², L. Webber³, K. Weber², W. Wehner³, X. Wei⁴⁸, D. Weisberg³, A. Welander³, A. Welsh⁴, A. White³⁷, R. Wilcox¹⁸, G. Wilkie², T. Wilks⁵, M. Willensdorfer⁹, H. Wilson¹⁶, A. Wingen¹⁸, M. Wu³¹, D. Wu³¹, S. Wukitch⁵, J. Xia⁵⁸, R. Xie¹², Z. Xing³, G. Xu³¹, X. Xu¹⁰, Z. Yan⁸, X. Yang⁷⁴, L. Yang⁵⁴, S. Yang², J. Yang², M. Yoo³, G. YU⁸⁰, J. Yu³, A. Zalzali¹⁹, A. Zamengo³, V. Zamkovska¹⁶, S. Zamperini³, K. Zarrabi³, E. Zeger¹³, K. Zeller³, L. Zeng¹³, X. Zhang³¹, J. Zhang³¹, B. Zhang³¹, J. Zhang³¹, B. Zhao¹², C. Zhao³, Y. Zheng⁸⁰, Y. Zhu⁸⁰, J. Zhu⁵, J. Ziegel¹², J. Zimmerman⁸, C. Zuniga³

¹ Lawrence Livermore National Laboratory, Livermore, CA, United States of America

² Princeton Plasma Physics Laboratory, Princeton, NJ, United States of America

³ General Atomics, San Diego, CA, United States of America

⁴ University of Tennessee, Knoxville, TN, United States of America

⁵ Massachusetts Institute of Technology, Boston, MA, United States of America

⁶ UiT The Arctic University of Norway, Tromsø, Norway

⁷ National Institutes for Quantum Science and Technology, Naka, Japan

⁸ University of Wisconsin, Madison, WI, United States of America

⁹ Max-Planck Institute for Plasma Physics, Garching, Germany

¹⁰ Lawrence Livermore National Laboratory, Livermore, CA, United States of America

¹¹ Imperial College London, London, United Kingdom

¹² University of Texas, Austin, TX, United States of America

¹³ University of California, Los Angeles, CA, United States of America

¹⁴ United Kingdom Atomic Energy Authority, Abingdon, United Kingdom

¹⁵ University of California, San Diego, CA, United States of America

¹⁶ Columbia University, New York, NY, United States of America

¹⁷ University of Denver, Denver, CO, United States of America

¹⁸ Oak Ridge National Laboratory, Oak Ridge, TN, United States of America

¹⁹ Oak Ridge Associated Universities, Oak Ridge, TN, United States of America

²⁰ Eindhoven University of Technology, Eindhoven, Netherlands

²¹ Consorzio RFX, Padua, Italy

²² Princeton University, Princeton, NJ, United States of America

²³ Purdue University, West Lafayette, IN, United States of America

²⁴ Brigham Young University, Provo, UT, United States of America

²⁵ NVIDIA, Santa Clara, CA, United States of America

²⁶ French Alternatives Energies and Atomic Energy Commission (CEA), Cadarache, France

²⁷ General Atomics Temp, San Diego, CA, United States of America

²⁸ College of William and Mary, Williamsburg, VA, United States of America

²⁹ Self-Employed

³⁰ Carnegie Mellon University, Pittsburgh, PA, United States of America

³¹ Institute for Plasma Physics, Chinese Academy of Sciences, Hefei, China

³² Tech-X Corporation, Boulder, CO, United States of America

³³ CompX, Del Mar, CA, United States of America

³⁴ Culham Centre for Fusion Energy, Abingdon, United Kingdom

³⁵ West Virginia University, Morgantown, WV, United States of America

³⁶ Sandia National Lab, Livermore, CA, United States of America

³⁷ Auburn University, Auburn, AL, United States of America

³⁸ Seoul National University, Seoul, Korea, Republic Of

³⁹ Swiss Federal Institute of Technology (EPFL), Lausanne, Switzerland

⁴⁰ Stanford Linear Accelerator Center, Norco, CA, United States of America

⁴¹ Commonwealth Fusion Systems, Devens, MA, United States of America

⁴² Xantho Technologies, LLC, Madison, WI, United States of America

⁴³ University of Illinois, Urbana-Champaign, IL, United States of America

⁴⁴ Istituto di Fisica del Plasma CNR-EURATOM, Milan, Italy

⁴⁵ Lawrence Berkeley National Laboratory, Berkeley, CA, United States of America

⁴⁶ ITER Organization, St. Paul-lez-Durance, France

⁴⁷ ENS Paris Saclay, Gif-sur-Yvette, France

⁴⁸ University of California, Irvine, CA, United States of America

⁴⁹ University of Toronto, Toronto, ON, Canada

⁵⁰ Portland State University, Portland, OR, United States of America

⁵¹ University of Michigan, Ann Arbor, MI, United States of America

⁵² Palomar Scientific Instruments, Inc, San Marcos, CA, United States of America

- ⁵³ University of Seville, Seville, Spain
⁵⁴ Lehigh University, Bethlehem, PA, United States of America
⁵⁵ Aalto University, Espoo, Finland
⁵⁶ Brown University, Providence, RI, United States of America
⁵⁷ Institute of High Performance Computing, Singapore
⁵⁸ University of Washington, Seattle, WA, United States of America
⁵⁹ ExoFusion, Bellevue, WA, United States of America
⁶⁰ Institute of Plasma Physics Chinese Academy of Sciences, Hefei, China
⁶¹ University of California, Santa Barbara, CA, United States of America
⁶² San Diego Mesa College, San Diego, CA, United States of America
⁶³ University of York, Heslington, United Kingdom
⁶⁴ Fiat Lux, San Diego, CA, United States of America
⁶⁵ Ghent University, Ghent, Belgium
⁶⁶ VTT Technical Research Centre, Espoo, Finland
⁶⁷ University of Colorado, Boulder, CO, United States of America
⁶⁸ The Pennsylvania State University, State College, PA, United States of America
⁶⁹ Chalmers University of Technology, Gothenburg, Sweden
⁷⁰ Ulsan National Institute of Science and Technology, Ulsan, Korea, Republic Of
⁷¹ Georgia Tech, Atlanta, GA, United States of America
⁷² University of Sao Paulo, Institute of Physics, Sao Paulo, Brazil
⁷³ Jefferson Lab, Newport News, VA, United States of America
⁷⁴ Dalian University of Technology, Dalian City, China
⁷⁵ Oak Ridge Institute for Science and Education, Oak Ridge, TN, United States of America
⁷⁶ Korean Advanced Institute of Science and Technology, Daejeon, Korea, Republic Of
⁷⁷ Hiroshima University, Hiroshima, Japan
⁷⁸ Bowdoin College, Brunswick, ME, United States of America
⁷⁹ National Institute for Fusion Science, Toki, Japan
⁸⁰ University of California, Davis, CA, United States of America
⁸¹ Zap Energy Inc, Seattle, WA, United States of America
⁸² National Fusion Research Institute, Daejeon, Korea, Republic Of
⁸³ Retired from General Atomics, San Diego, CA, United States of America

E-mail: holcomb6@llnl.gov

Received 27 November 2023, revised 9 February 2024

Accepted for publication 4 March 2024

Published 15 August 2024



Abstract

The DIII-D tokamak has elucidated crucial physics and developed projectable solutions for ITER and fusion power plants in the key areas of core performance, boundary heat and particle transport, and integrated scenario operation, with closing the core-edge integration knowledge gap being the overarching mission. New experimental validation of high-fidelity, multi-channel, non-linear gyrokinetic turbulent transport models for ITER provides strong confidence it will achieve $Q \geq 10$ operation. Experiments identify options for easing H-mode access in hydrogen, and give new insight into the isotopic dependence of transport and confinement. Analysis of 2,1 islands in unoptimized low-torque IBS demonstration discharges suggests their onset time occurs randomly in the constant β phase, most often triggered by non-linear 3-wave coupling, thus identifying an NTM seeding mechanism to avoid. Pure deuterium SPI for disruption mitigation is shown to provide favorable slow cooling, but poor core assimilation, suggesting paths for improved SPI on ITER. At the boundary, measured neutral density and ionization source fluxes are strongly poloidally asymmetric, implying a 2D treatment is needed to model pedestal fuelling. Detailed measurements of pedestal and SOL quantities and impurity charge state radiation in detached divertors has validated edge fluid modelling and new self-consistent ‘pedestal-to-divertor’ integrated modeling that can be used to optimize reactors. New feedback adaptive ELM control minimizes confinement reduction, and RMP ELM suppression with sustained high core performance was obtained for the first time with the outer strike point in a W-coated, compact and unpumped small-angle slot divertor. Advances have been made in integrated operational scenarios for ITER and power plants. Wide pedestal intrinsically

ELM-free QH-modes are produced with more reactor-relevant conditions, Low torque IBS with W-equivalent radiators can exhibit predator-prey oscillations in T_e and radiation which need control. High- β_P scenarios with $q_{\min} > 2$, $q_{95} \sim 7.9$, $\beta_N > 4$, $\beta_T \sim 3.3\%$ and $H_{98y2} > 1.5$ are sustained with high density ($\bar{n} = 7E19 \text{ m}^{-3}$, $f_G \sim 1$) for $6 \tau_E$, improving confidence in steady-state tokamak reactors. Diverted NT plasmas achieve high core performance with a non-ELMing edge, offering a possible highly attractive core-edge integration solution for reactors.

Keywords: DIII-D, tokamak, overview

(Some figures may appear in colour only in the online journal)

1. Introduction

The DIII-D tokamak research program utilizes a favourable combination of fusion-relevant size, flexible and varied actuators, and outstanding diagnostics to provide scientific solutions for ITER and FPPs. Program achievements in the last two years discussed in the paper range from focused and detailed physics model validation studies to broad scope integrated operational scenario development, and address processes from the core plasma to divertor surfaces and the main chamber walls. Results fall into three general categories that are the organizational basis for the paper: section 2 highlights investigations of requirements for high core plasma performance, including transport, confinement, stability, and disruption mitigation; section 3 covers boundary heat and particle transport studies, including understanding and optimizing the pedestal, fuelling, divertors, and impurity influx; and section 4 reports integrated operational scenarios for ITER and FPPs, including ELM control solutions, burn control, high-performance steady states, and NT. Conclusions and discussion of future possibilities for research on DIII-D are discussed in section 5.

2. Requirements for high core performance

Accurate prediction of ITER and FPP operation and their potential fusion performance is needed, and recent DIII-D experiments shed light on transport, confinement, stability, and disruption mitigation important for these devices. Extensive high-resolution measurements of kinetic profiles (n_e , T_e , T_i , n_C), turbulence fluctuations (low-wavenumber (low-k) n_e and T_e), and impurity transport (Li, C, and Ca) were collected in ITER-similar shaped plasmas designed to examine multi-channel transport in relevant conditions ($q_{95} = 3.45$, low rotation, and ELM-suppressed H-mode). These data showed excellent agreement with machine-learning-assisted nonlinear gyrokinetic CGYRO [1] predictive simulations [2]. Machine learning helps to predict converged CGYRO solutions, reducing the computational cost by a factor of 4–6. The basic approach detailed in [2] is to run four local CGYRO simulations between $\rho = 0.3$ and $\rho = 0.8$ on a set of randomly generated profiles around the experimental conditions, and then to produce a surrogate model based on these simulations capturing the dependence of fluxes on known turbulence drives.

New profiles are then predicted by the surrogate model to match measured fluxes, and these are input to new CGYRO runs—if these match experimental fluxes the profiles are considered converged. Pedestal top values are taken from experiment. Figure 1 shows the T_i , T_e , and n_e , and n_C (carbon) profiles were all reproduced within the scatter of the experimental measurements by the ion-scale nonlinear gyrokinetic simulation that matches experimental heat and particle fluxes, and there is good agreement between predicted and measured low-k density fluctuations (figure 2). This validation motivated the use of these new techniques to project and optimize performance in ITER conditions. The same modeling framework predicts ITER should achieve the primary goal of $Q \sim 10$ with ~ 500 MW of fusion power and suggests paths for further enhancement. Additional simulations predict ITER should still be able to achieve burning plasma conditions with RMP ELM suppression and degraded pedestal conditions.

Before ITER can achieve $Q = 10$ it must progress through non-nuclear commissioning phases, so DIII-D has developed better solutions for H-mode access in hydrogen and deepened understanding of energy confinement dependence on ion mass. Experiments in ITER-similar shaped hydrogen plasmas with ion collisionality at $\rho \sim 0.95$ a factor of 2–4 higher than expected in ITER L-modes at $B_T = 1.8$ T have demonstrated that the L-H power threshold P_{LH} can be reduced via applied $n = 3$ NRMP using the external C-coil [3]. NRMP produces counter-current torque in the plasma edge via NTV, driving edge toroidal rotation that increases the local ExB shear inside the separatrix, reducing P_{LH} by 25%–30%. This reduction is observed for plasmas with balanced NBI (simulating ITER) as well as for finite NBI torque. MARS-F plasma response calculations for low density ITER hydrogen plasmas predict that significant counter- I_p torque can be generated with optimum phasing of the ITER 3D coil system just inside the ITER last closed flux surface. On DIII-D, P_{LH} is also found to decrease 20%–50% by initiating H-mode at lower I_p ; the observed hysteresis between L-H and H-L power thresholds in hydrogen suggests ITER could trigger H-mode in the I_p -ramp-up and sustain it into flat-top. Impurity seeding has also been shown to reduce P_{LH} using Helium in DIII-D, with up to 15% seeding reducing P_{LH} by 10%–20%, and up to 25% seeding reducing P_{LH} by 30%–35% (figure 3) [3]. Intrinsic carbon impurity dilution also reduces P_{LH} in hydrogen and deuterium plasmas at low edge collisionality compared to ‘pure’ hydrogen plasmas

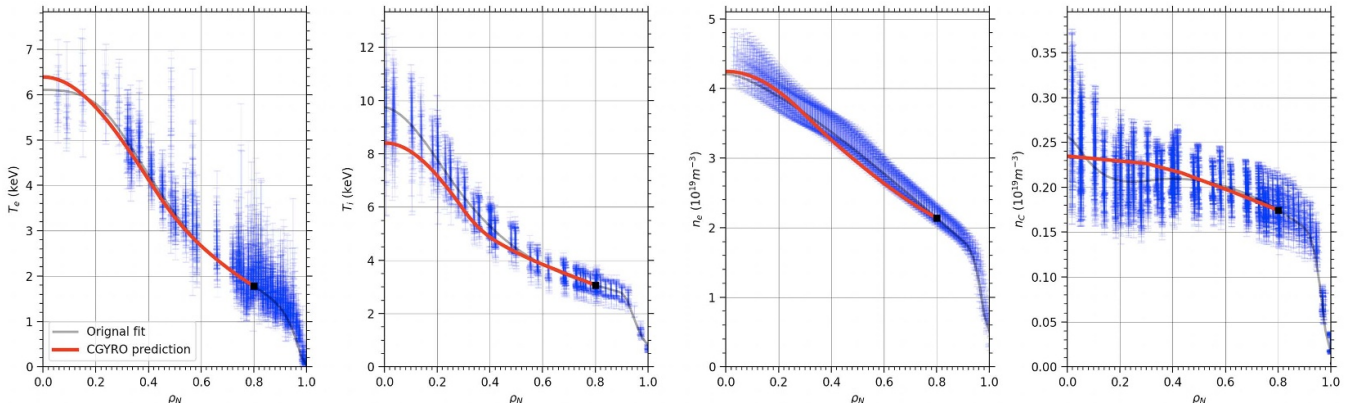


Figure 1. Machine learning assisted nonlinear CGYRO transport code profile predictions match measurements.

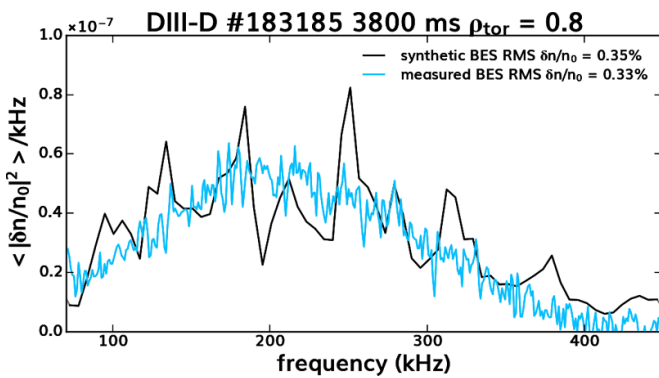


Figure 2. Machine learning assisted nonlinear CGYRO accurately predicts the measured beam emission spectroscopy density fluctuation cross power spectrum.

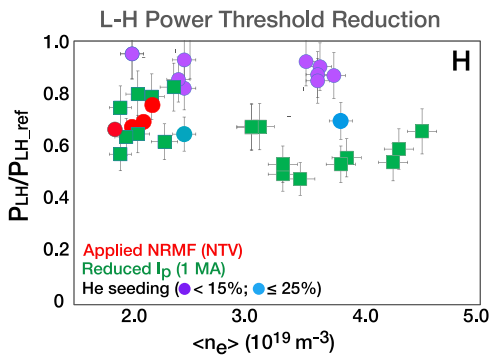


Figure 3. The L-H power threshold is reduced using low-Z seeding, NRMF, and reduced I_p .

with very low $Z_{\text{eff}} \sim 1.25$ (figure 4) [4]. TGLF [5] gyro-fluid and CGYRO gyrokinetic simulations indicate main ion carbon dilution causes an upshift in the ITG critical gradient. In addition, electron non-adiabaticity effects contribute to the higher power threshold in hydrogen compared to deuterium. The dependence of the ITG critical gradient on ion dilution potentially allows the reduction of P_{LH} during ITER hydrogen campaigns via N or Ne light impurity seeding.

New measurements of the detailed turbulence characteristics in dimensionally similar hydrogen and deuterium plasmas

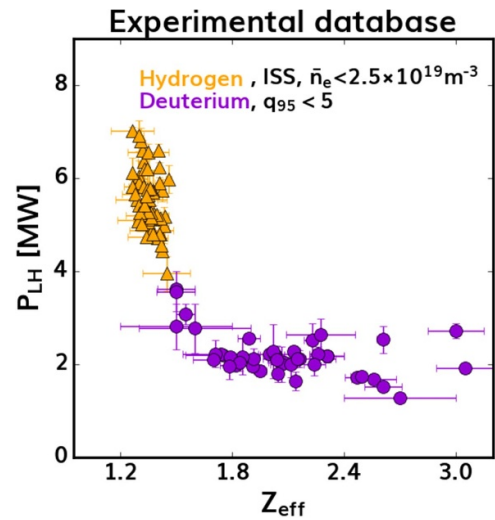


Figure 4. Main ion dilution by carbon reduces the L-H power threshold.

partially explain the significant differences in transport and energy confinement time with isotope mass [6], complimenting similar studies done on JET and ASDEX-U [7–9]. Energy confinement τ_E is well known to be higher in deuterium (D) than hydrogen (H); in the specific ITER-shaped ELMy H-mode plasmas heated by NBI and ECH in this study, τ_E of the D plasmas exceeded that in H by a factor of ~ 1.8 . The D and H plasmas had well matched β , safety factor q , and pedestal and core T_e/T_i profiles while normalized gyroradius ρ^* and collisionality ν^* varied. In contrast, BES measurements of low wavenumber ($k_{\perp} \rho_i < 1$) turbulent density fluctuations show the amplitude is higher in D than H, with similar spectral structure, in the radial range $0.35 < \rho < 0.8$. While this is consistent with gyroBohm predictions of normalized fluctuation amplitude scaling as $\rho^* \sim$ square root of mass [10], it is apparently at odds with the observed higher τ_E with mass. However, the BES measurements show H has significantly higher radial correlation length than D, ~ 3.8 cm compared to ~ 2.4 cm (figure 5). This contradicts the gyroBohm prediction that the correlation length should also scale as ρ^* , and it offers a potential explanation for enhanced transport

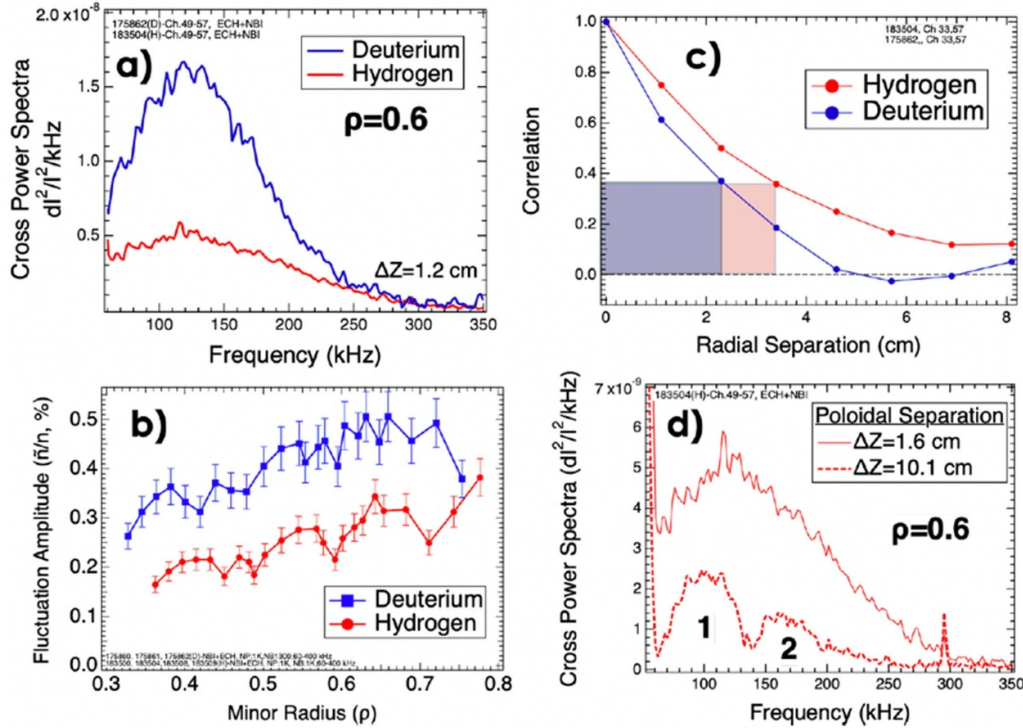


Figure 5. BES measurements: (a) density fluctuation spectra, (b) fluctuation amplitude profile, (c) radial correlation length, and (d) poloidally separated spectra for hydrogen only showing secondary mode.

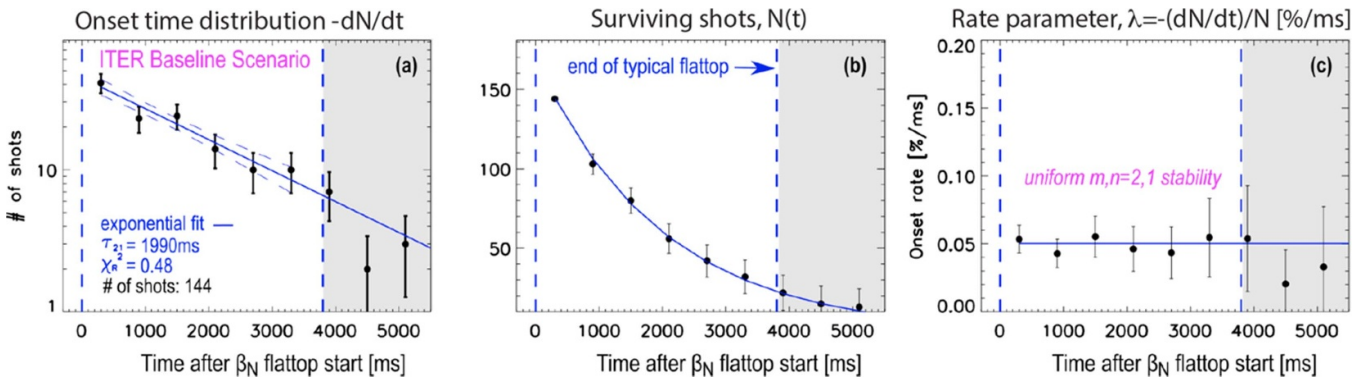


Figure 6. $M/n = 2/1$ mode onset distribution analysis for unstable ITER Baseline Scenario demonstration discharges.

and reduced confinement with lower ion mass because random walk diffusivity scales as the square of the correlation length. BES measurements also show H but not D has a low-to-intermediate wavenumber mode with longer poloidal correlation length but lower amplitude (figure 5(d)). These transport physics insights show differences in core turbulence are at least partially responsible for ion mass confinement scaling, and these will help validate nonlinear simulations and confinement projections of D-T plasmas in ITER and other future devices.

MHD stability and disruption avoidance is a fundamental requirement for ITER and all tokamak-based power plants. A particular focus is DIII-D demonstration low-torque IBS discharges. Scenario control sequences that reliably and

systematically favor either stable or unstable 2/1 operation for the duration of the I_p flattop exist [11, 12]. The stable sequence includes delayed heating and gas flow to regularize ELMs, resulting in a different current profile at the start of the $\beta_N = 1.8$ phase that modeling predicts is farther from ideal kink and classical tearing limits. For IBS discharges that develop a 2/1 mode, the unstable database onset time distribution in the constant β_N phase is well fit by an exponential, meaning 2/1 mode onsets follow Poisson point-process statistics and have a constant onset rate $\lambda = -(dN/dt)/N$, where N is the number of surviving discharges up to time t . (figure 6) [13]. Such an onset time distribution is inconsistent with the modes being triggered by purely classical effects the same way in all discharges, i.e. classical stability index Δ' evolving above a

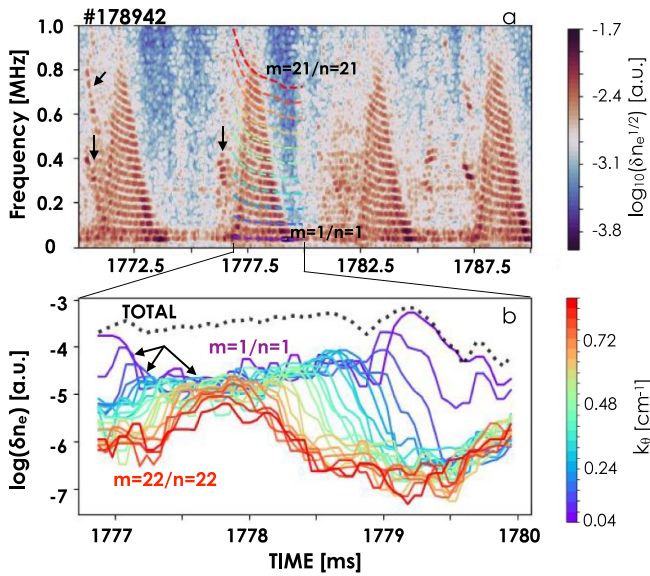


Figure 7. (a) Fluctuation spectra measured by reflectometry at the $q = 1$ flux surface. Right before each burst, the noticeable amplitudes of \tilde{n} and \tilde{B} in the intermediate k range are briefly destabilized, as indicated by arrows in (a). The peak-to-peak frequency spacing in the staircase-shaped frequency spectra is 32 kHz (indicated by arrows), close to the frequency at the end of the chirping of the lowest k_θ wave, i.e. 31.5 kHz. Third arrow points to ~ 0.2 – ~ 0.4 MHz medium- k modes. (b) Time evolution of the perturbations along the dashed lines in (a), corresponding to the mode number from $m = 1/n = 1$. To $m = 22/n = 22$. The color represents different wave numbers.

critical value in ~ 1 resistive diffusion time, because modeling predicts this would result in λ peaking at some time, which is not observed. Poisson statistics imply seeding is happening at random times, and this is consistent with the observation of 3-wave coupling [14] in a majority of 2/1-unstable IBS discharges, whereby 2/1's are triggered by sawtooth precursors coupling to 3/2 islands when differential rotation between rational surfaces approaches zero. Rotation flattening occurs with temporally uniform probability due to $n > 1$ activity. This shows the importance of properly controlling multiple quantities to help avoid 2/1 modes in ITER.

In experiments with ~ 10 keV thermal ions minor disruptions are triggered by multi-scale chirping modes associated with the $q = 1$ surface when T_i exceeds a threshold, which is well below the predicted ideal β_N limit [15]. Analysis of magnetic and density fluctuation spectra indicates a strong non-linear interaction between medium- k and low- k waves. Linear analysis with CGYRO suggest the medium- k modes (e.g. see the third arrow pointing to ~ 0.2 to ~ 0.4 MHz fluctuations in figure 7(a)) are kinetic ballooning/electromagnetic Alfvén ITG modes resonating with thermal ions on passing orbits. MARS-K [16] suggests the lowest- k mode (e.g. lowest frequency 1/1 mode shown in purple in figure 7(b)) has a mix of kink and tearing eigenstructure, resonating with thermal ions on trapped orbits [17]. This initially local structure can expand from local to global in ~ 0.5 ms (faster than NTM

growth) causing edge islands, current profile redistribution, a moderate drop in I_p , a substantial density spike, impurity influx, and loss of edge temperature. These results confirm that mode resonances with hot thermal tail ions in reactors will be important, and further study is needed to assess mitigations.

Experiments deploying SPI inform new optimizations of this technique for disruption mitigation on ITER. Previous studies indicated that mixed or staggered low- and high- Z injection may be required to effectively mitigate thermal loads and RE [18]. New experiments tested the staggered approach with spatially and temporally resolved density and temperature profiles after pure D_2 injection, and mixed Ne/ D_2 injection [19]. This used upgrades to the Thomson scattering diagnostic to enable measurements at ~ 1 eV (new narrow-band polychromators), asynchronous triggering by pellet ablation light, and ‘burst mode’ close sequential firing of the lasers to capture fast dynamics. A single shattered pellet injector on the low field side close to the Thomson scattering measurements was used. Pure D_2 SPI produces a favorable ten or more millisecond delay to the disruption, but very limited core fueling is observed before the disruption. Even during and after the disruption, when strong mixing of the injected material with the plasma is expected, the edge density significantly exceeds the core density. 1D INDEX [20] transport modeling suggests the poor assimilation is caused by strong outward ∇B induced drift of the ablation cloud and predicts larger pellet shards with higher pellet speed will improve D_2 assimilation (figure 8). Greater speed alone is less effective because it usually results in smaller fragments. The mixed ($\sim 50:50$) Ne/ D_2 pellet impacts are dominated by Ne; these cause fast radiative collapse of the plasma in a few milliseconds and almost uniform density profile once Ne mixes during and after the thermal quench.

New comparison of DIII-D infrared imaging measurements of the inner wall to kinetic orbit RE code (KORC) modeling indicates that SEEs produced by the RE avalanche source at energies below the runaway threshold energy are the primary contributor to transient surface heating of PFCs during final loss events of RE mitigation [21]. The KORC simulations use an analytical first wall for modeling a non-axisymmetric first wall composed of individual tiles; a method was added to approximately include gyrophase to guiding center orbits intersecting PFCs to enable accurate calculations of angle of incidence needed to determine volumetric energy deposition. Simulations show initial REs with significant energy drifts remain confined, even when passing, in magnetic configurations connected to the first wall during the final loss event. But SEEs born at lower energies, below the runaway threshold energy, with little energy drift can be rapidly lost to the first wall (figure 9). Qualitative agreement between simulations and infrared imaging is obtained only when SEEs are included. Some observed differences between the modeled heating and the IR images are likely due to differences in the time resolutions of modeling and imaging, and possibly due to differences in the temperature

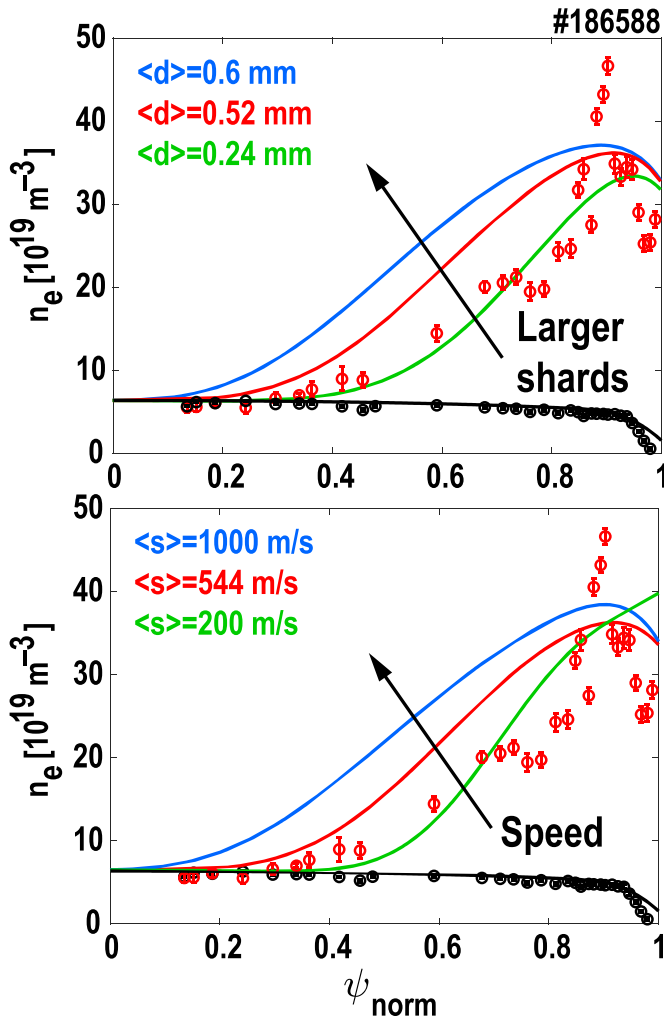


Figure 8. INDEX modeling (curves) compared to density measurements (points) for D2 SPI.

saturation levels of the two. Since typical predictions of PFC heating due to REs only consider high-energy REs, these results provide an important new guideline, showing the need to consider SEE to fully predict potential wall damage.

3. Boundary heat and particle transport

Studies using DIII-D have elucidated important physics and developed new controls related to the plasma edge and first wall. Novel Lyman-alpha diagnostic measurements [22] show a significant poloidal variation of the main chamber edge ionization source. A one order of magnitude HFS-LFS fueling asymmetry exists when operating with ion $B \times \nabla B$ drift towards the X-point; in this case the fueling is greatest on the HFS. Operating with ion $B \times \nabla B$ drift out of the divertor results in higher fueling on the LFS, but with a factor ~ 2 asymmetry. (figure 10) [23]. The ionization source asymmetries are related to asymmetric recycling fluxes at the inner and outer divertor targets due to directional parallel plasma

flows in the scrape-off layer. Gyrokinetic-plasma and kinetic-neutral simulations using the XGC suite of total-f particle-in-cell codes [24] and DEGAS2 Monte Carlo neutral transport calculations [25] reproduce these observations [26]. The parallel plasma flow in the scrape-off-layer is driven primarily by particle orbit and collisional physics, while turbulent transport across the separatrix determines the overall magnitude. That is, while neutral fueling asymmetries appear in ‘neoclassical’ simulations that exclude turbulence, quantitative agreement between simulations and experiment is only found when the turbulent particle losses are included. Analysis of these simulations indicate that a low-recycling edge plasma results in novel flow patterns, which cause neutrals to be dominantly produced on one or the other divertor plates. In a highly collisional scrape-off layer as expected in burning plasma devices with larger spatial scale and higher connection length a symmetrization of the parallel plasma fluxes is expected and, therefore, recycling fluxes and main chamber ionization source are expected to become HFS-LFS symmetric. Still, these results motivate at least 2D modeling to understand fueling in present devices.

DIII-D experimental validation of a new integrated model of the pedestal-to-divertor system enables prediction of pedestal pressures and heat flux widths in future devices. The combined EPED-SOLPS modeling framework was used to predict DIII-D pedestal pressure and width, ion flux to the divertor, and the electron temperature at the divertor target over a range of pedestal density as the divertor was pushed into detachment (figure 11) [27]. Measurements of these quantities match the predicted trends with increasing density reasonably well. The model predicted pedestal pressure rate of decrease with density is captured, while pedestal width is nearly constant and quantitatively matched. Predicted and measured ion flux to the divertor reach their peak values at the onset of detachment at roughly the same pedestal density, and target temperatures agree quantitatively, indicating the model accurately predicts the detachment onset density. Accounting for both pedestal and SOL physics in the integrated modeling accurately predicts the pedestal pressure is ballooning limited throughout the density scans, consistent with the generally low pressure observed, while standalone EPED [28] calculations predict a transition from peeling-limited to ballooning-limited at a higher density than what is observed. One important addition to the integrated model is the option to use an empirical relationship between the divertor temperature from SOLPS [29] and the ratio of pedestal to separatrix densities used by EPED. Using this relation obviates the need to have the pedestal density as an input parameter to the model. Similar agreement between experiment and modeling was achieved in three different divertor closure geometries on DIII-D. Bolstered by this validation, the integrated modeling framework is being used to predict pedestals and peak heat flux in proposed FPP. In these predictive simulations, EPED predicted profiles and the sources derived from the combined model yield transport coefficients in the closed flux region, and a pair of SOL width models, either the Eich model [30] or a ballooning-critical SOL model, are used to determine coefficients in the SOL.

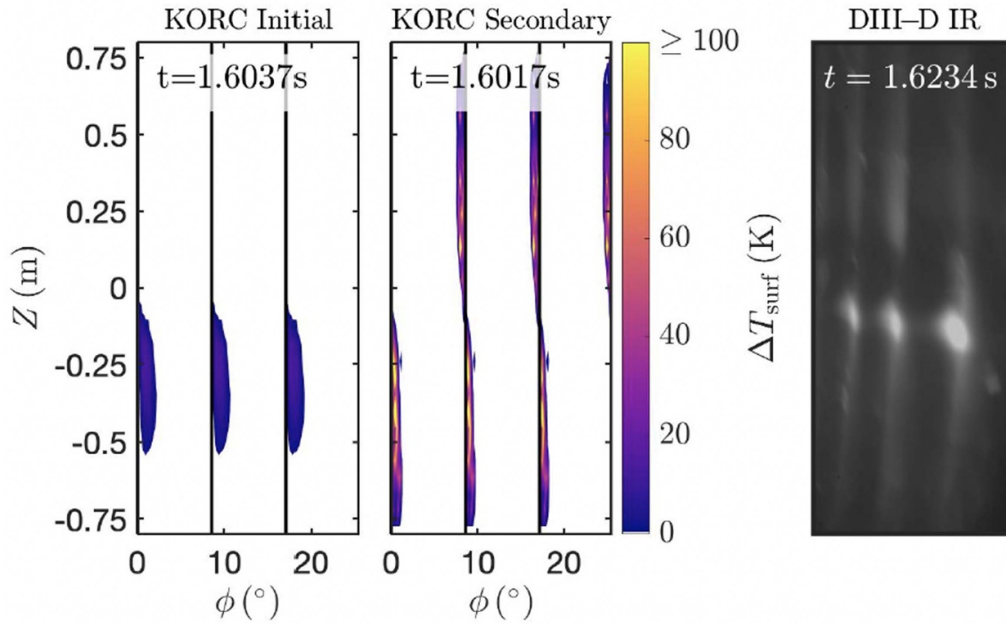


Figure 9. KORC modelling of inner wall tile edge heating by energetic electrons matches IR camera measurements only when subcritical electrons are included (middle panel).

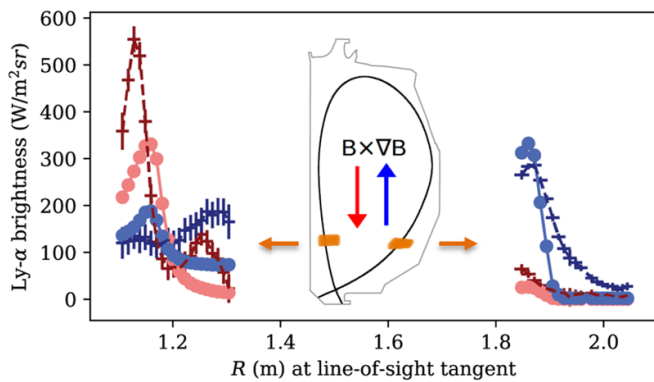


Figure 10. Lyman-alpha measurements (crosses) compared to XGC1-DEGAS2 simulation (circles) for ion Bxgrad(B) into X-point (red) and out of X-point (blue). Inset shows measurement locations.

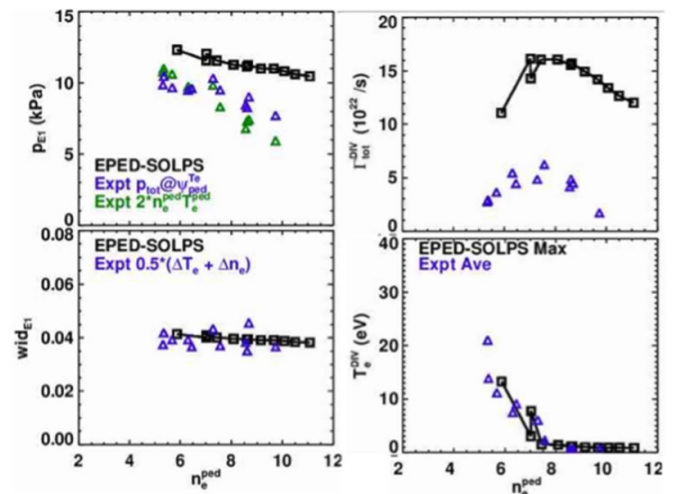


Figure 11. Measurement and predictive EPED-SOLPS modeling of pedestal pressure and width, divertor ion flux and electron temperature.

Either the empirical relationship between the ratio of pedestal to separatrix density can be used, or the pedestal density can be taken as an input parameter. Initial FPP predictions find that in some cases the predicted pedestal height from the combined model is significantly higher than that predicted by standalone EPED.

Prediction of detachment in radiative divertor regimes requires validated models of mixed impurity transport and radiation dependence on density, temperature, and P_{SOL} . New 2D multi-wavelength experimental data has been compared to 2D full-drift-physics modeling in single and mixed impurity plasmas with good agreement found [31]. For model validation, it is essential to match the charge state distributions of impurities, which depend on T_e , to accurately predict radiated power density throughout the divertor region. A set of multiple

absolutely calibrated spectroscopic and imaging diagnostics in visible and EUV/VUV spectral regions were combined to determine both carbon (C) and nitrogen (N) multi-charge-state divertor concentrations and radiative power constituents in conditions ranging from attached to fully detached. These were compared to 2D UEDGE [32] fluid simulations with full particle drifts and charge state resolved C and N impurities included. The UEDGE simulations match experimentally resolved 2D divertor Te and reproduced the dominant divertor radiated power sources from VUV resonance transitions of C II—C IV and N II—N V, as well as the relative contributions from C and N to the total divertor radiation

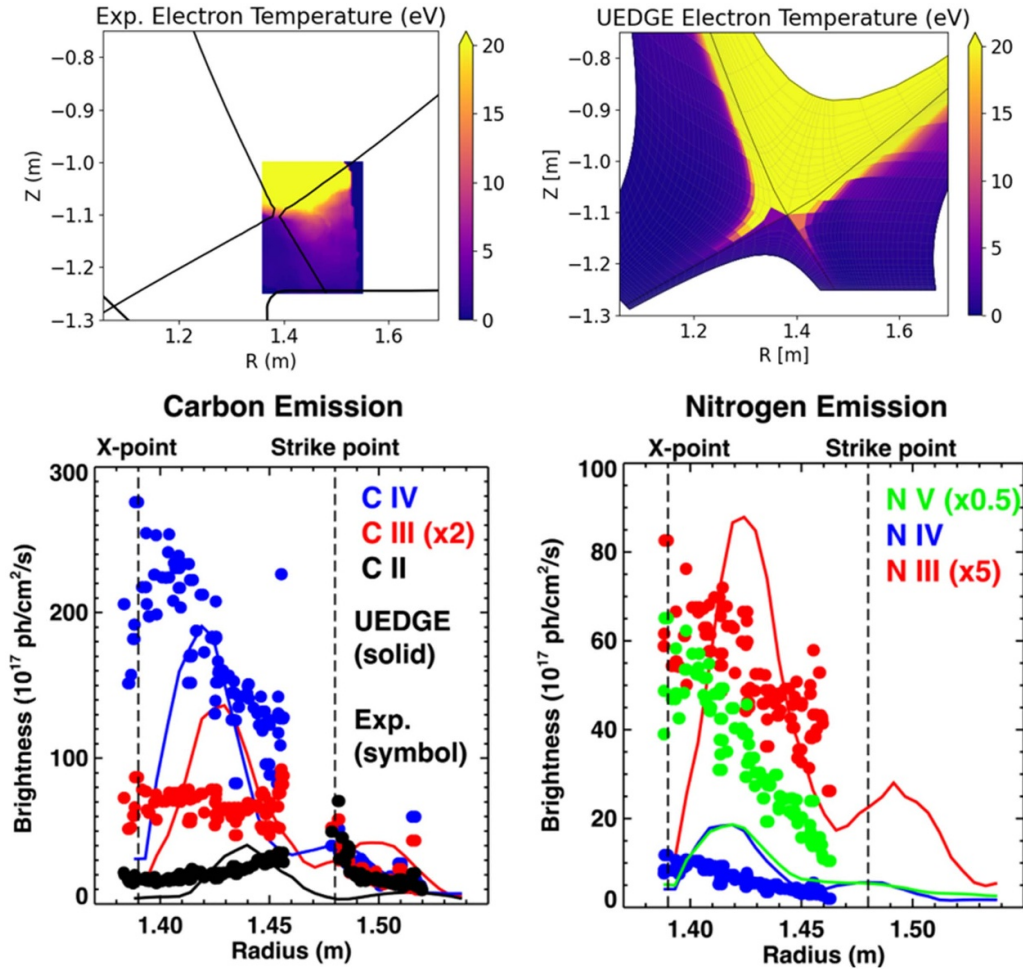


Figure 12. UEDGE modeling compared to measured T_e (top) and C and N emission (bottom) in the divertor region.

(figure 12). These results provide confidence in the application of these models to design radiative divertor solutions for future devices.

A new feedback-adaptive RMP ELM suppression control algorithm was tested on DIII-D and KSTAR that provides a new solution for ELM control in reactors (figure 13) [33]. Typically, open loop RMP ELM control with fixed 3D coil currents sufficient for suppressing Type-I ELMs results in degraded pedestal pressure and τ_E . The new algorithm applies a predetermined coil current I_{RMP} while the discharge is still in L-mode and maintains this through transition to H-mode to avoid all ELMs. Then, the algorithm reduces I_{RMP} while monitoring deuterium-alpha signals for ELMs. In KSTAR, ELM precursor events are detected [34], but so far these have not been seen in DIII-D. Upon detection of a precursor or an ELM, the controller sets a new lower limit for I_{RMP} , increases I_{RMP} to recover suppression, and then attempts to lower it again iteratively. Minimization of $n = 3$ I_{RMP} increases τ_E in DIII-D test cases by $\sim 18\%$ relative to τ_E in H-mode with the higher predetermined I_{RMP} .

Separately, pedestal control and performance has been expanded in two novel regimes. A robust range of counter- I_p edge rotation was found in which density increases with

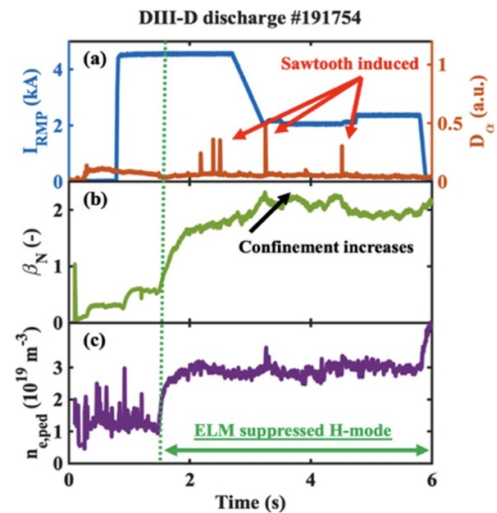


Figure 13. Feedback adaptive $n = 3$ RMP ELM suppression minimizes confinement degradation.

applied $n = 2$ RMP still below the suppression threshold. This is opposite to the well-known density pump out usually observed with RMP that tends to reduce global performance.

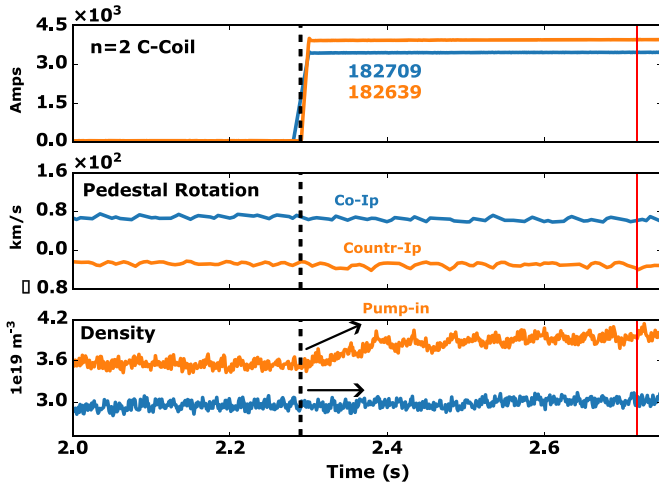


Figure 14. RMP with edge counter- I_p rotation (orange) raises particle confinement.

The greatest line-density increase is about 15% and occurs with a counter- I_p pedestal rotation of $\sim 40 \text{ km s}^{-1}$. (figure 14, [35]). Doppler back scattering measurements show the prompt increase in particle confinement is due to a drop in inter-ELM pedestal turbulence amplitude and a switch from an ion- to electron-mode at the pedestal top. The other new development is the application of counter- I_p ECCD at the pedestal to reduce the required RMP amplitude for ELM suppression. This results in a higher pedestal pressure with the same τ_E and is a useful tool for pedestal physics exploration [36].

RMP ELM suppression has previously been demonstrated in the Tungsten (W) divertor of ASDEX-U with a vertical target configuration [37]. On DIII-D these studies are extended to the narrow, W-coated small-angle slot unpumped divertor, which is shown to be compatible with RMP ELM suppression and core W control in a similar parameter space. Experiments evaluated the impacts of ELM control on H-mode plasmas with $q_{95} = 3.75$ and an outer strike point in the SAS-VW divertor (see the inset of figure 16) [38, 39]. Without any ELM control, ELMs dominate the W source that contaminates the core plasma. The ELMs, and therefore the W source, tend to be larger with greater plasma stored energy W_{MHD} and lower pedestal collisionality ν_{ped}^* . ELM mitigation and in some cases full suppression (figure 15) with $n = 3$ RMPs significantly reduce or eliminate the W source per ELM at high W_{MHD} and low ν_{ped}^* (figure 16). Higher W_{MHD} and lower ν_{ped}^* are observed to be approximately constant for the duration of the ELM suppressed phase in the I_p flat-top ($\sim 1.5 \text{ s}$), indicating that W transport out of the core is still sufficiently high to avoid W build-up despite loss of ELMs, which are also known to flush impurities. These results suggest RMP ELM suppression integrated with a narrow W slot divertor is a solution capable of maintaining high fusion performance with minimal PFC damage in future reactors.

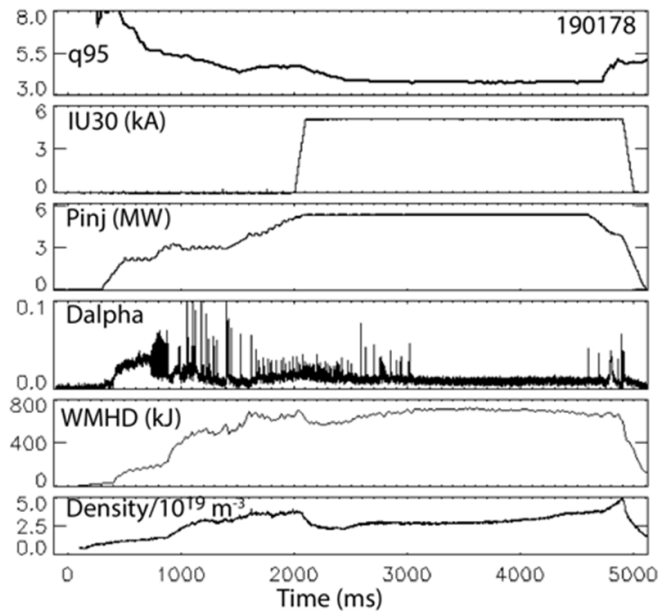


Figure 15. Time traces of an ELM suppressed ($n = 3$ RMP) discharge with outer strike point on a W-coated small angle slot divertor.

4. Integrated operational scenarios

A high-level program goal is to put core and edge solutions together for sustained high performance with sufficient heat and particle exhaust and without damaging transients like ELMs. Several paths are being pursued to provide such operational scenarios for ITER and FPPs along with discerning the key physics requirements of each.

Significant progress has been made in expanding the operational space and physics understanding of Quiescent H-mode (QH-mode) as a promising naturally ELM-stable high-performance scenario for reactors (figure 17) [40]. The range of q_{95} of WPQH operating at low torque ($< 1.5 \text{ Nm}$) has recently been reduced to 4.2, which is the lowest yet achieved for this scenario in a quasi-stationary state. Separately, the maximum heating power WPQH-mode can take before the reappearance of ELMs has been increased from 5.5 MW to 7.5 MW. This is limited by the available balanced NBI power to keep the net torque small. WPQH at net-zero injected torque has been achieved in both directions of I_p , with both favorable and unfavorable ion $B \times \nabla B$ drift directions, and in different plasma shapes including an ITER-like shape. Recently, WPQH-modes were produced in hydrogen plasmas with $Z_{\text{eff}} \sim 2$. This is notable because deuterium WPQH-mode plasmas typically have high Z_{eff} due to carbon wall sputtering; the lower Z_{eff} in hydrogen, likely due to lower carbon physical sputtering [41], demonstrates high Z_{eff} is neither necessary nor inevitable in this scenario. WPQH-modes are observed to lack the standard H-mode ion-channel power degradation of τ_E [42]. Extensive transport modeling using TGYRO/TGLF

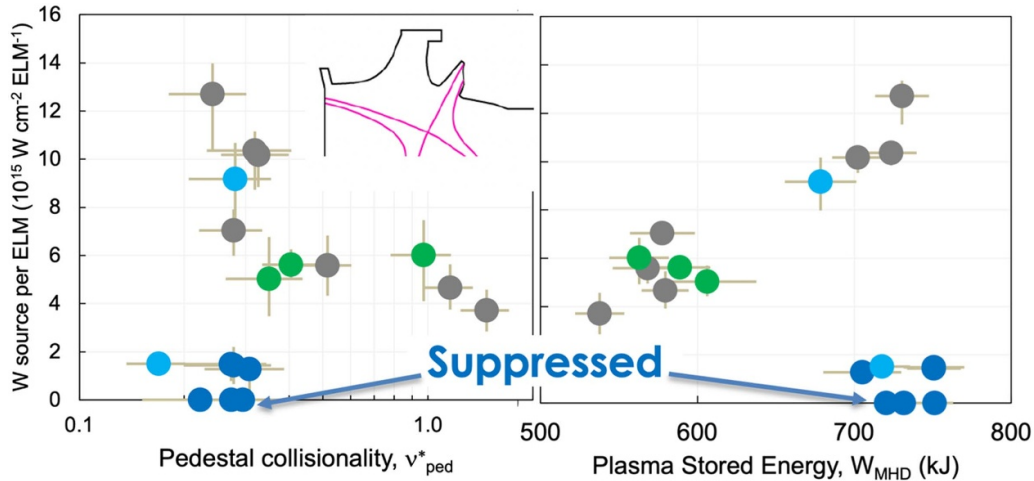


Figure 16. Measured W source per ELM versus pedestal collisionality and plasma stored energy. Inset shows the upper divertor geometry with the OSP in a W -coated small angle slot. Gray dots: no ELM control, green: pellet injection, light blue: $n = 2$ RMP, dark blue: $n = 3$ RMP.

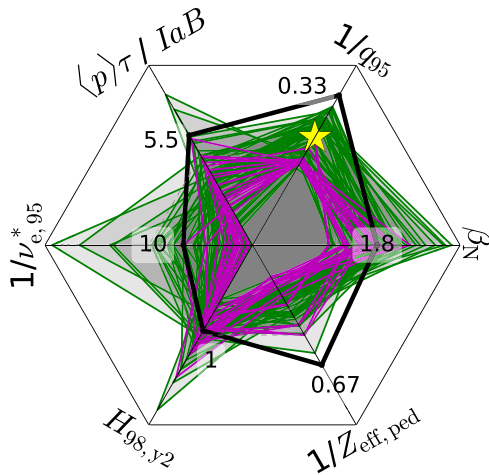


Figure 17. Radar plot showing key metrics for IBS ($Q = 10$), black lines, and achieved QH- and WPQH-mode DIII-D discharges. The yellow star indicates new lower q_{95} (4.2) WPQH-mode.

shows that this could be explained by the large Shafranov shift in these plasmas stabilizing core drift-wave instabilities and enabling high-confinement ELM-stable plasmas [43]. A low $E \times B$ shear region in the middle of the pedestal is thought to allow the destabilization of broadband MHD and/or turbulence observed there. Detailed analyses and numerical modeling of pedestal instabilities identify one mild peeling-ballooning mode and one drift-Alfvén wave that compete to produce the wide pedestal [44]. The divertor heat width λ_q of ‘turbulent’ QH-mode plasmas is observed (figure 18) to increase with edge broadband MHD/turbulence with cases where λ_q exceeds Eich scaling [45]. Modeling indicates this is associated with turbulence spreading across the separatrix [46].

DIII-D tested the impacts of W radiation on the burn phase of the IBS by using W -equivalent radiators [47]. Kr and Xe mixtures have the same radiative loss rates L_z in the DIII-D core as W in the hotter ITER core, so they are injected

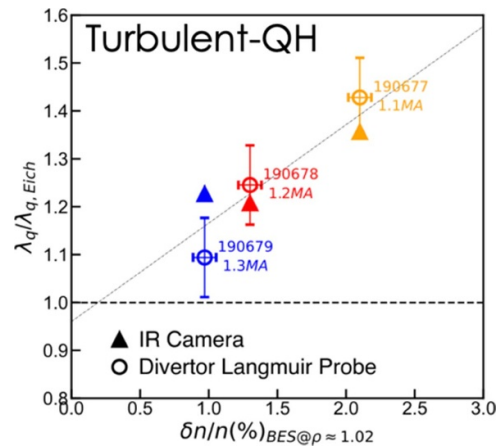


Figure 18. Measured ratio of heat flux width to Eich-scaling-predicted heat flux width versus normalized edge density fluctuation for turbulent QH-modes.

as proxies to simulate the impacts of W radiation in ITER. IBS demonstration plasmas were generated with these radiators (figure 19) spanning the range of expected impurity concentration and W radiated fraction with net NBI torque scanned between 0 and 5 Nm. Impurity concentrations of $n_{Kr}/n_e \sim 2 \times 10^{-4}$ and $n_{Xe}/n_e \sim 6 \times 10^{-5}$ correspond to ITER expected $n_W/n_e \sim 1e-5$ and $f_{rad} \sim 30\%$ (given DIII-D’s lower density than ITER). In the range of $f_{rad} = 0.25$ – 0.35 , a bifurcation is observed, which either allows the scenario to be stationary, or trigger an oscillatory regime with T_e and f_{rad} oscillating out of phase, and the core oscillating out of phase from the edge/pedestal. A Lotka–Volterra predator-prey model with full profiles, diffusion, and noise was designed to gain insight into the dynamics of the system, and its results show that this model can reproduce the experimental T_e and f_{rad} profiles. To explore the more specific physics of a tokamak plasma and extrapolate to ITER, a physics-based model not constrained to oscillate was designed

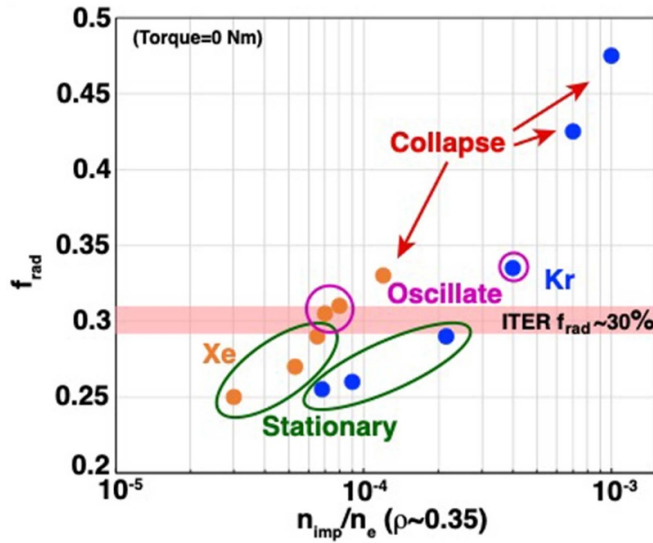


Figure 19. IBS radiation fraction versus impurity concentration using W-equivalent radiators.

that successfully reproduces the oscillatory behavior of the experiment, with the correct range of amplitude and phase difference observed, remaining robustly stable to variations in inputs. This indicates a reasonable understanding of the drivers of this phenomenon for projecting to ITER, as well as mimicking alpha power and burn dynamics in DIII-D. Future DIII-D experiments will aim at controlling burn phase oscillations.

The High- β_P Scenario for steady-state operation with high fusion gain and high bootstrap current fraction (f_{BS}) has been optimized for improved MHD stability. One advance is the use of a novel variable-poloidal-spectrum mode control with internal non-axisymmetric coils (I-coils) [48]. A high- β_P regime is often investigated on DIII-D using slow continued ramps of I_P and/or B_T throughout the discharge, resulting in varying q_{95} . The new feedback scheme configures the upper and lower I-coil rows in two independent feedback loops, allowing the feedback field poloidal spectrum to vary and track changes in the plasma mode structure over a range of q_{95} from 6 to 11. The q_{95} dependence of the observed phase difference between the coil rows during feedback is qualitatively compatible with ideal MHD simulations of the least-stable plasma kink mode. This feedback facilitated high β_N operation in excess of the ideal MHD $n = 1$ no-wall kink stability limit, with a broad current profile and low internal inductance, $\beta_P = 3$, and $f_{BS} \approx 60\%$. Such performance extensions, particularly to lower internal inductance ℓ_i (figure 20), are not obtained using coupled coil rows. Variable-spectrum feedback helps avoid beta collapses caused by marginally stable RWM activity. These results underscore the utility of MHD mode control for accessing high- β fusion-relevant regimes. The variable spectrum feedback approach is a straightforward way to improve resilience to variations in mode structure that occur as plasma parameters change. The extension to lower ℓ_i is expected to improve the coupling of the

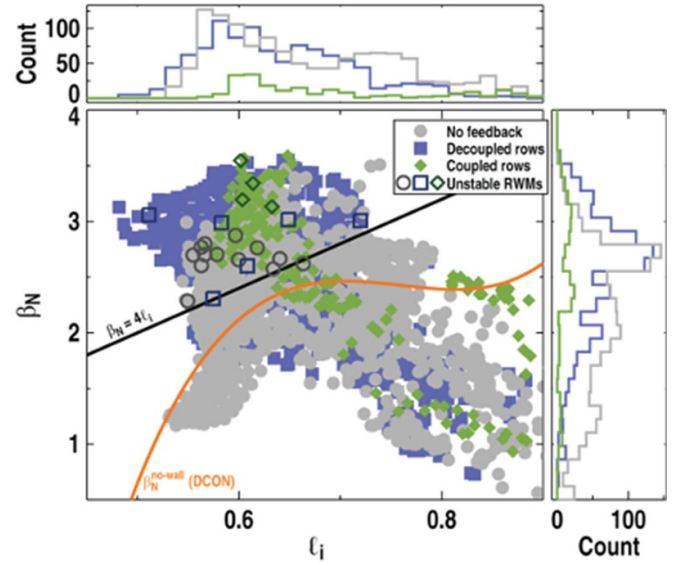


Figure 20. New RWM feedback with independent (i.e. decoupled) I-coil rows compared to standard feedback and no feedback in the High-Beta-Poloidal scenario.

plasma kink mode to external (i.e. feedback) fields and beneficial wall eddy currents, and is compatible with high- f_{BS} operation.

In a few High- β_P Scenario discharges, further tuning of the ramp-up sequence to optimize the current and pressure profiles has resulted in higher performance sustained for longer [49]. $\beta_N \sim 4.2$ ($\sim 6\ell_i$), $\beta_T \sim 3.3\%$, and $q_{min} > 2$ was sustained for ~ 0.7 of a current profile relaxation time (more than $6 \tau_E$), with $f_{BS} \sim 80\%$, a large-radius internal transport barrier, $H_{98y2} \sim 1.7$, line-averaged $f_{Gr} \sim 1$, and stationary impurity levels (figure 21). The high-performance phase is terminated by fast growing modes destabilized at the $n = 1$ ideal MHD, ideal-wall kink stability limit, following transient β_N excursions above the feedback-controlled target. A rapidly growing $n = 1$ mode appears as the limiting instability during one of these excursions, preventing stationary sustainment of high performance. GATO [50] calculations indicate that the plasma is crossing the ideal-wall $n = 1$ kink limit right before the disruption. New microwave and RF capabilities for off-axis current drive (top launch EC [51], helicon [52], high field side lower hybrid [53]) could remove the need for a low- β -phase B_T ramp down and high- β -phase slow I_P ramp up to achieve fully noninductive operation with improved coupling between modes and the wall, thus increasing the ideal-wall β_N limit. Improved β_N feedback controls are being developed to avoid transient excursions above the target. These results improve confidence that the High- β_P Scenario is an attractive option for steady-state operation in ITER and power plants.

DIII-D carried out a multiple-week campaign in 2023 to investigate NT [54], building upon previous results from TCV [55] and DIII-D [56]. Graphite-tile armor was installed on the low-field-side lower outer wall to obtain high power unpumped diverted plasmas with strong NT (figure 22(a)).

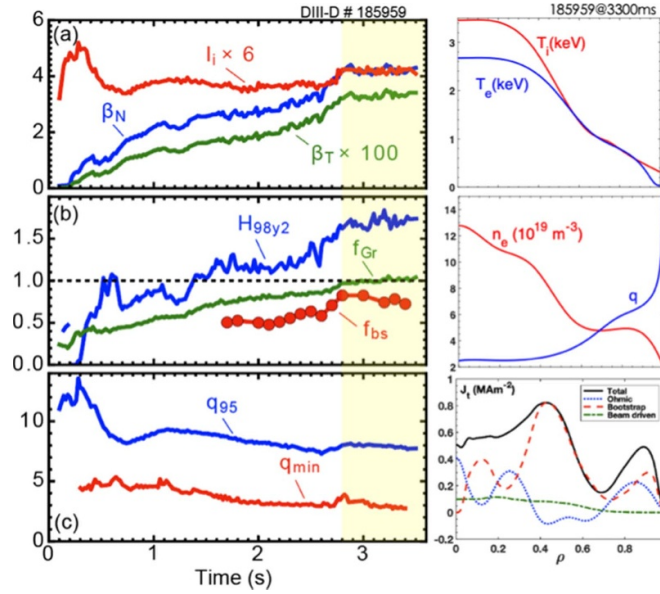


Figure 21. Time histories and profiles at $t = 3.3$ s for the High-Beta-Poloidal scenario optimized for high performance.

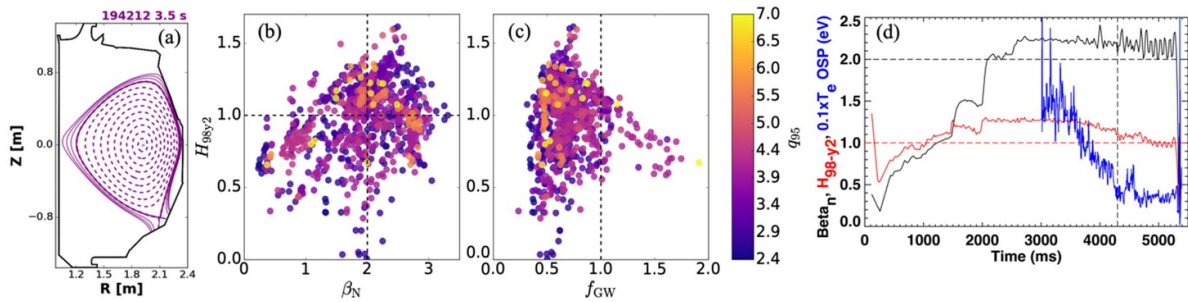


Figure 22. (a) NT shape with armored tiles. (b) and (c) show H_{98y2} , β_N , and density limit fraction f_G for a range of q_{95} averaged over 400 ms stationary periods. (d) β_N , H_{98y2} , and outer strike point T_e in NT detached discharge.

High confinement ($H_{98y2} \geq 1$), high current ($q_{95} < 3$), and high normalized pressure ($\beta_N > 2.5$) plasmas were achieved at high-injected-power in a strong NT-shape with a lower outer divertor X-point that also demonstrated high normalized line-density ($n_e/n_G \leq 2$) and a detached divertor without ELMs. The L-H transition was inhibited at $\delta_{avg} = -0.5$ at all injected beam powers (up to 12 MW) and torques possibly due to restricted second stability access from infinite- n ballooning modes predicted in NT [57, 58]. However, while not an H-mode edge, there is slight T_e pedestal compared to L-mode plasmas, resulting in the so-called NT-edge. A range of discharges were studied from high gain cases with $q_{95} = 2.7$, to cases with $q_{95} = 4$ and 50%–60% non-inductive current. Both cases achieved high performance ($\beta_N > 2.5$ and $H_{98y2} \sim 1$, figure 22(b)). In NBI-heated plasmas, high central densities up to $n_{e0} \sim 1.4 \times 10^{20} \text{ m}^{-3}$ and high Greenwald fractions f_G approaching 2 were achieved, whereas in plasmas with only Ohmic heating f_G was limited to 1 (figure 22(c)). Divertor detachment was obtained (figure 22(d)) in density ramps with only D_2 injection in both favorable and unfavorable ion $B \times \nabla B$ drift directions [59]. This showed a more gradual L-mode-like detachment evolution with no detachment cliff [60].

Plasma shaping limitations result in relatively short parallel connection length between the midplane and divertor target, and this leads to detachment requiring very high density and f_G . The highest f_G detached cases have reduced energy confinement correlated with loss of T_e -pedestal and uncontrolled X-point radiation moving up the HFS edge. Overall, the NT-campaign results demonstrate several key principles indicating the potential viability of NT as the basis for a fusion power plant [61].

5. Future plans and conclusions

The DIII-D program plans several hardware upgrades between now and 2028 that will better enable it to close key knowledge gaps for a successful ITER program and design of FPP. These include increases in flexible heating and current drive power in parallel with testing a series of new divertor designs and new technologies. Raising ECH and current drive delivered power from 5 MW in 2024 to 14 MW in 2028 is key for testing ITER and FPP integrated scenario physics with relevant higher T_e/T_i , lower torque, lower fast ion fraction,

lower collisionality, and higher density in a range of inductive and non-inductive equilibria. New high harmonic fast wave (Helicon) and high-field-side launched Lower Hybrid systems coming online will further enhance DIII-D's ability to achieve and test advanced scenarios with broad current and pressure profiles for high β_N steady-state operation in higher density plasmas. The divertor stages will start with a new relatively small-volume closed divertor optimized for a large volume highly shaped core plasma predicted to enable high peeling-limited pedestal pressures at low collisionality and reactor-relevant pedestal neutral opacity. This will be succeeded by a larger Stage-2 slot-like divertor with sufficient volume for detailed radiative heat dissipation and detachment studies with moderate shaping. Divertor Stage 3 will be optimized to integrate high core performance with efficient and capable heat and particle exhaust. Stage-3 will arrive in 2028 when upgrades to ECH, RF, and NBI systems are complete, providing up to ~ 43 MW total heating power. Planning is underway to design a NT-optimized pumped divertor and new plasma shaping that would extend NT studies, including to longer connection length and lower detachment density for higher confinement. Along the way, DIII-D will develop technologies: an ECH gyrotron test socket is planned, along with dedicated vacuum ports to test new reactor-relevant diagnostics and first wall materials. The novel helicon and high-field-side lower hybrid systems will be further developed, as well as disruption mitigation systems like shell pellets designed to reach and cool the core from the inside out [62], and a passive 3D coil designed to deconfine and render harmless RE [63].

In conclusion, research on DIII-D is finding solutions for fusion energy. It has provided tools and identified essential requirements for achieving high core fusion performance. These include validated turbulent transport models capable of predicting kinetic profiles, new understanding of the isotopic dependence of turbulence, and the demonstration of methods to ease H-mode access in ITER's non-nuclear phases. Harmful MHD instability causes have been diagnosed and new guidance for instability avoidance and disruption mitigation provided. Research on DIII-D has elucidated boundary heat dissipation and particle fuelling processes that need to be understood and controlled for successful fusion energy. These include assessments of ionization source asymmetries, validation of a model for pedestal and heat flux behaviors during detachment, and characterization of mixed impurity concentrations needed to dissipate power into the SOL. Also, RMP ELM control was shown to mitigate Tungsten contamination, and feedback controlled RMPs were shown to minimize confinement degradation during suppression. Finally, DIII-D has put a range of integrated operational scenarios on a firmer basis. Naturally ELM-free wide pedestal quiescent H-mode operation has been extended to a larger range of reactor relevant conditions, and IBSs have been tested with Tungsten equivalent radiators to study and control stationary- and oscillating-temperature regimes that result. For steady-state operation, the High- β_P Scenario has reached higher β_N with lower ℓ_i using new scenario controls. NT has been shown to be capable of high performance with a non-ELMing edge

and divertor detachment, offering a novel option for future fusion reactors.

Acknowledgments

This material is based upon work supported by the U.S. Department of Energy, Office of Science, Office of Fusion Energy Sciences, using the DIII-D National Fusion Facility, a DOE Office of Science user facility, under Awards DEFC02-04ER54698 and DE-AC52-07NA27344.

Disclaimer

This report was prepared as an account of work sponsored by an agency of the United States Government. Neither the United States Government nor any agency thereof, nor any of their employees, makes any warranty, express or implied, or assumes any legal liability or responsibility for the accuracy, completeness, or usefulness of any information, apparatus, product, or process disclosed, or represents that its use would not infringe privately owned rights. Reference herein to any specific commercial product, process, or service by trade name, trademark, manufacturer, or otherwise does not necessarily constitute or imply its endorsement, recommendation, or favoring by the United States Government or any agency thereof. The views and opinions of authors expressed herein do not necessarily state or reflect those of the United States Government or any agency thereof.

Appendix. Glossary of acronyms

BES	beam emission spectroscopy
ECH	electron cyclotron heating
ECCD	electron cyclotron current drive
ELM	edge localized mode
EUV	extreme ultraviolet
FPP	fusion pilot plant
HFS	high-field side
IBS	ITER baseline scenario
ITG	ion temperature gradient
LFS	low-field side
NBI	neutral beam injection
NRMP	non-resonant magnetic perturbations
NTM	neoclassical tearing mode
NT	negative triangularity
NTV	neoclassical toroidal viscosity
PFS	plasma-facing component
QH-mode	quiescent high-confinement mode
RE	runaway electrons
RF	radiofrequency
RMP	resonant magnetic perturbation
RWM	resistive wall mode
SEE	subcritical energetic electrons
SOL	scrape off layer
SPI	shattered pellet injection
VUV	vacuum ultraviolet
WPQH	wide-pedestal quiescent H-mode

References

- [1] Candy J., Belli E.A. and Bravenec R.V. 2016 A high-accuracy eulerian gyrokinetic solver for collisional plasmas *J. Comput. Phys.* **324** 73
- [2] Howard N. 2023 Performance and transport in ITER: multi-channel validation in DIII-D ITER-like conditions and predictions of ITER burning plasmas via nonlinear gyrokinetic profile prediction *Preprint submitted: 2023 IAEA Fusion Energy Conf. (London)* [EX/3-4]
- [3] Schmitz L. 2023 Accessing and maintaining robust H-mode in ITER pre-fusion power operation (PFPO) plasmas *Preprint submitted: 2023 IAEA Fusion Energy Conf. (London)* [EX/P7-4]
- [4] Callahan K. 2023 Origin of the L-H threshold isotope effect in DIII-D hydrogen and deuterium plasmas *Preprint submitted: 2023 IAEA Fusion Energy Conf. (London)* [EX/P4-10]
- [5] Staebler G., Kinsey J.E. and Waltz R.E. 2007 A theory-based transport model with comprehensive physics *Phys. Plasmas* **14** 055909
- [6] Mckee G. 2023 Turbulence, transport and confinement dependence on isotope mass in dimensionally similar H-mode plasmas on DIII-D *Preprint submitted: 2023 IAEA Fusion Energy Conf. (London)* [EX/3-2]
- [7] Schneider P. *et al* 2017 Explaining the isotope effect on heat transport in L-mode with the collisional electron-ion energy exchange *Nucl. Fusion* **57** 066003
- [8] Maggi C. *et al* 2018 Isotope effects on L-H threshold and confinement in tokamak plasmas *Plasma Phys. Control. Fusion* **60** 014045
- [9] Molina Cabrera P., Rodriguez-Fernandez P., Görler T., Bergmann M., Höfler K., Denk S.S., Bielajew R., Conway G.D., Yoo C. and White A.E. 2023 Isotope effects on energy transport in the core of ASDEX-Upgrade tokamak plasmas: turbulence measurements and model validation *Phys. Plasmas* **30** 082304
- [10] Mckee G. *et al* 2001 Non-dimensional scaling of turbulence characteristics and turbulent diffusivity *Nucl. Fusion* **41** 1235
- [11] Turco F., Luce T.C., Solomon W., Jackson G., Navratil G.A. and Hanson J.M. 2018 The causes of the disruptive tearing instabilities of the ITER baseline scenario in DIII-D *Nucl. Fusion* **58** 106043
- [12] Turco F. *et al* 2024 Modelling and experiment to stabilize the ITER baseline scenario in DIII-D *Nucl. Fusion* **64** 076048
- [13] Bardoczi L. 2023 The root cause of disruptive NTMs and paths to stable operation in DIII-D ITER baseline scenario plasmas *Preprint submitted: 2023 IAEA Fusion Energy Conf. (London)* [EX/P7- 1669]
- [14] Bardoczi L., Logan N. and Strait E. 2021 Neoclassical tearing mode seeding by nonlinear three-wave interactions in tokamaks *Phys. Rev. Lett.* **127** 055002
- [15] Du X. *et al* 2021 Multiscale chirping modes driven by thermal ions in a plasma with reactor-relevant ion temperature *Phys. Rev. Lett.* **127** 025001
- [16] Liu Y., Chu M.S., Chapman I.T. and Hender T.C. 2008 Toroidal self-consistent modeling of drift kinetic effects on the resistive wall mode *Phys. Plasmas* **15** 112503
- [17] Liu Y., Xie W. and Du X. 2022 Modelling of thermal-ion-driven internal kink in DIII-D high-Ti plasmas *Nucl. Fusion* **62** 086050
- [18] Lehnen M. *et al* 2022 *Paper presented at 2nd IAEA Technical Meeting on Disruptions and their Mitigation (19–22 July 2022)* (available at: <https://conferences.iaea.org/event/281/contributions/24711/>)
- [19] Lvovskiy A., Matsuyama A., O’Gorman T., Shiraki D., Herfindal J.L., Hollmann E.M., Marini C., Boivin R., Eidietis N.W. and Lehnen M. 2024 Density and temperature profiles after low-Z and high-Z shattered pellet injections on DIII-D *Nucl. Fusion* **64** 016002
- [20] Matsuyama A., Hu D., Lehnen M., Nardon E. and Artola J. 2022 Transport simulations of pre-thermal quench shattered pellet injection in ITER: code verification and assessment of key trends *Plasma Phys. Control. Fusion* **64** 105018
- [21] Beidler M. 2024 Wall heating by subcritical energetic electrons generated by the runaway electron avalanche source *Nucl. Fusion* **64** 076038
- [22] Rosenthal A. *et al* 2021 A 1D Lyman-alpha profile camera for plasma edge neutral studies on the DIII-D tokamak *Rev. Sci. Instrum.* **92** 033523
- [23] Laggner F. 2023 Disentangling H-mode pedestal structure and neutral ionization source *Preprint submitted: 2023 IAEA Fusion Energy Conf. (London)* [EX/P7-29]
- [24] Ku S.H. *et al* 2018 A fast low-to-high confinement mode bifurcation dynamics in the boundary-plasma gyrokinetic code XGC1 *Phys. Plasmas* **25** 056107
- [25] Stotler D. and Karney C. 1994 Neutral gas transport modeling with DEGAS 2 *Contrib. Plasma Phys.* **24** 392
- [26] Wilkie G. 2023 Kinetic simulations of pedestal fuelling asymmetry and implication for scrape-off layer flows *Preprint submitted: 2023 IAEA Fusion Energy Conf. (London)* [TH/3-2]
- [27] Snyder P. 2023 Self-consistent integrated modeling of the pedestal, scrape-off layer, and divertor *Preprint submitted: 2023 IAEA Fusion Energy Conf. (London)* [TH/P7-122]
- [28] Snyder P., Groebner R.J., Hughes J.W., Osborne T.H., Beurskens M., Leonard A.W., Wilson H.R. and Xu X.Q. 2011 A first-principles predictive model of the pedestal height and width: development, testing, and ITER optimization with the EPED model *Nucl. Fusion* **51** 103016
- [29] Wiesen S. *et al* 2015 The new SOLPS-ITER code package *J. Nucl. Mater.* **463** 480
- [30] Eich T. *et al* 2013 Scaling of the tokamak near the scrape-off layer H-mode power width and implications for ITER *Nucl. Fusion* **53** 093031
- [31] Scotti F. 2023 2D characterization of radiative divertor regimes with impurity seeding in DIII-D H-mode discharges *Preprint submitted: 2023 IAEA Fusion Energy Conf. (London)* [EX/8-4]
- [32] Rognlien T., Milovich J.L., Rensink M.E. and Porter G.D. 1992 A fully implicit, time dependent 2D fluid code for modeling tokamak edge plasmas *J. Nucl. Mater.* **196** 347
- [33] Shousha R. 2023 Closed loop RMP ELM suppression with minimized confinement degradation using adaptive control demonstrated in DIII-D and KSTAR *Preprint submitted: 2023 IAEA Fusion Energy Conf. (London)* [IFE/1-4]
- [34] Kim S. *et al* 2022 Optimization of 3D controlled ELM-free state with recovered global confinement for KSTAR with $n=1$ resonant magnetic field perturbation *Nucl. Fusion* **62** 026043
- [35] Logan N. *et al* 2022 Improved particle confinement with resonant magnetic perturbations in DIII-D tokamak H-mode plasmas *Phys. Rev. Lett.* **129** 205001
- [36] Logan N., Lyons B.C., Knolker M., Hu Q., Cote T. and Snyder P. 2024 Access to stable, high pressure tokamak pedetals using local electron cyclotron current drive *Nucl. Fusion* **64** 014003
- [37] Suttrop W. *et al* 2018 Experimental conditions to suppress edge localised modes by magnetic perturbations in the asdex upgrade tokamak *Nucl. Fusion* **58** 096031

- [38] Abrams T. 2023 Unravelling the physics of tungsten sourcing and leakage from a slot divertor configuration on DIII-D *Preprint submitted: 2023 IAEA Fusion Energy Conf. (London)* [TH/P7-28]
- [39] Abrams T. *et al* 2021 Design and physics basis for the upcoming DIII-D SAS-VW campaign to quantify tungsten leakage and transport in a new slot divertor geometry *Phys. Scr.* **96** 124073
- [40] Chen X. 2023 Recent progress of the reactor-relevant intrinsically ELM-stable quiescent H-mode on the DIII-D tokamak *Preprint submitted: 2023 IAEA Fusion Energy Conf. (London)* [EX/2-3]
- [41] Eckstein W. *et al* 1993 Sputtering Data Report IPP9/82 Max Planck Institut für Plasmaphysik Garching
- [42] Chen X. *et al* 2020 Expanding the parameter space off the wide-pedestal QH-mode towards ITER conditions *Nucl. Fusion* **60** 092006
- [43] Houshmandyar S., Burrell K.H., Grierson B.A., McClenaghan J., Staebler G.M., Chrystal C., Halfmoon M.R., Hatch D.R., Zeng L. and Austin M.E. 2022 Explaining the lack of power degradation of energy confinement in wide pedestal quiescent H-modes via transport modelling *Nucl. Fusion* **62** 056024
- [44] Li Z. *et al* 2022 Numerical modeling of pedestal stability and broadband turbulence of wide-pedestal QH-mode plasmas on DIII-D *Nucl. Fusion* **62** 076033
- [45] Ernst D. *et al* 2023 Broadening of the divertor heat flux profile in high confinement tokamak fusion plasmas with edge pedestals limited by turbulence *Phys. Rev. Lett.* Submitted
- [46] Li Z. *et al* 2024 How turbulence spreading improves power handling in quiescent high confinement fusion plasmas *Commun. Phys.* **7** 96
- [47] Turco F. 2024 First tungsten radiation studies in DIII-D's ITER baseline demonstration discharges *Nucl. Fusion* **64** 076063
- [48] Hanson J. 2024 Variable-spectrum mode control of high poloidal beta discharges *Nucl. Fusion* **64** 086024
- [49] Huang J. 2023 Sustainment of High q_{\min} , High β_N Plasmas on DIII-D Towards Steady-State Advanced Tokamak Fusion *Preprint submitted: 2023 IAEA Fusion Energy Conf. (London)* [EX/7-5]
- [50] Bernard L., Helton F.J. and Moore R.W. 1981 GATO: an MHD stability code for axisymmetric plasmas with internal separatrices *Comput. Phys. Commun.* **24** 377
- [51] Chen X. *et al* 2022 Doubling off-axis electron cyclotron current drive efficiency via velocity space engineering *Nucl. Fusion* **62** 054001
- [52] Van Compernelle B. *et al* 2021 The high-power helicon program at DIII-D: gearing up for first experiments *Nucl. Fusion* **61** 116034
- [53] Leppink S., Lau C., Lin Y. and Wukitch S.J., 2023 Development of DIII-D high field side lower hybrid current drive launcher *2023 IAEA Fusion Energy Conf. (London)* [TEC/P5- 2108] p 94
- [54] Thome K. 2023 Assessment of negative triangularity as a reactor scenario in DIII-D *2023 IAEA Fusion Energy Conf. (London)* [EX/1-2]
- [55] Camenen Y., Pochelon A., Behn R., Bottino A., Bortolon A., Coda S., Karpushov A., Sauter O., Zhuang G. and team T.T. 2007 Impact of plasma triangularity and collisionality on electron heat transport in TCV L-mode plasmas *Nucl. Fusion* **47** 510
- [56] Austin M. *et al* 2019 Achievement of reactor-relevant performance in negative triangularity shape in the DIII-D tokamak *Phys. Rev. Lett.* **122** 115001
- [57] Nelson A. *et al* 2023 Robust L-mode edge behaviour in high performance negative triangularity plasmas: from experiments to reactors *Preprint submitted: 2023 IAEA Fusion Energy Conf. (London)* [EX/P7-31]
- [58] Saarelma S., Austin M.E., Knolker M., Marinoni A., Paz-Soldan C., Schmitz L. and Snyder P.B. 2021 Ballooning instability preventing the H-mode access in plasmas with negative triangularity shape on the DIII-D tokamak *Plasma Phys. Control. Fusion* **63** 105006
- [59] Scotti F. *et al* 2024 High performance power handling in the absence of an H-mode edge in negative triangularity DIII-D plasmas *Nucl. Fusion* **64** 094001
- [60] Jaervinen A. *et al* 2018 $E \times B$ flux driven detachment bifurcation in the DIII-D tokamak *Phys. Rev. Lett.* **121** 075001
- [61] Kikuchi M. *et al* 2019 L-mode-edge negative triangularity tokamak reactor *Nucl. Fusion* **59** 056017
- [62] Izzo V. 2023 Simulations of shell pellet injection strategies for ITER-scale tokamaks *Plasma Phys. Control. Fusion* **65** 095007
- [63] Izzo V. 2023 Runaway electron prevention by a passive 3D coil in disruption simulations of the SPARC and DIII-D tokamaks *Preprint submitted: 2023 IAEA Fusion Energy Conf. (London)* [EX/3-4]